J. Fluid Mech. (2010), *vol.* 650, *pp.* 287–306. © Cambridge University Press 2010
doi:10.1017/S0022112009993570

On bubble clustering and energy spectra in pseudo-turbulence

JULIÁN MARTÍNEZ MERCADO†,
DANIEL CHEHATA GÓMEZ,
DENNIS VAN GILS,
CHAO SUN AND DETLEF LOHSE

Physics of Fluids Group, Department of Science and Technology, J.M. Burgers Centre for Fluid Dynamics and IMPACT Institute, University of Twente, PO Box 217, 7500 AE Enschede, The Netherlands

(Received 21 April 2009; revised 20 November 2009; accepted 22 November 2009; first published online 24 March 2010)

Three-dimensional particle tracking velocimetry (PTV) and phase-sensitive constant temperature anemometry in pseudo-turbulence – i.e. flow solely driven by rising bubbles – were performed to investigate bubble clustering and to obtain the mean bubble rise velocity, distributions of bubble velocities and energy spectra at dilute gas concentrations ($\alpha \leqslant 2.2\,\%$). To characterize the clustering the pair correlation function $G(r, \theta)$ was calculated. The deformable bubbles with equivalent bubble diameter $d_b = 4$–5 mm were found to cluster within a radial distance of a few bubble radii with a preferred vertical orientation. This vertical alignment was present at both small and large scales. For small distances also some horizontal clustering was found. The large number of data points and the non-intrusiveness of PTV allowed well-converged probability density functions (PDFs) of the bubble velocity to be obtained. The PDFs had a non-Gaussian form for all velocity components and intermittency effects could be observed. The energy spectrum of the liquid velocity fluctuations decayed with a power law of -3.2, different from the $\approx -5/3$ found for homogeneous isotropic turbulence, but close to the prediction -3 by Lance & Bataille (*J. Fluid Mech.*, vol. 222, 1991, p. 95) for pseudo-turbulence.

1. Introduction

Bubbly pseudo-turbulence – i.e. a flow solely driven by rising bubbles – is relevant from an application point of view due to the omnipresence of bubble columns, e.g. in the chemical industry, in water treatment plants and in the steel industry (Deckwer 1992). A better understanding of the involved phenomena is necessary for scaling-up industrial devices and for optimization and performance prediction. This article aims to provide experimental data on pseudo-turbulence by means of novel experimental techniques. The main questions to be addressed are:

(i) What is the preferential range and the orientation of bubble clustering in pseudo-turbulence?

(ii) What is the mean bubble rise velocity and what kind of probability distribution does the bubble velocity have?

(iii) What is the shape of the energy spectrum of pseudo-turbulence?

† Email address for correspondence: j.martinezmercado@tnw.utwente.nl

https://doi.org/10.1017/S0022112009993570 Published online by Cambridge University Press

1.1. *Bubble clustering*

In dispersed flows, the hydrodynamic interaction between the two phases and the particle inertia result in an inhomogeneous distribution of both particles and bubbles (see e.g. experimentally Ayyalasomayajula *et al.* 2006; Salazar *et al.* 2008; Saw *et al.* 2008 and numerically Bec *et al.* 2006*a*; Calzavarini *et al.* 2008*a*,*b* and Toschi & Bodenschatz 2009 for a general recent review). Bubble clustering in pseudo-turbulence has been studied numerically (Sangani & Didwana 1993; Smereka 1993; Sugiyama, Takagi & Matsumoto 2001; Mazzitelli & Lohse 2009) and experimentally (Cartellier & Rivière 2001; Zenit, Koch & Sangani 2001; Risso & Ellingsen 2002; Roig & de Tournemine 2007). The numerical work by Smereka (1993) and by Sangani & Didwana (1993) and theoretical work by van Wijngaarden (1993), Kok (1993) and van Wijngaarden (2005) suggest that, when assuming potential flow, rising bubbles form horizontally aligned rafts. Three-dimensional direct numerical simulations (DNS), which also solve the motion of the gas–liquid interface at the bubble's surface, have become available in the last few years. The works by Bunner & Tryggvason (2002*a*, 2003) suggest that the deformability effect plays a crucial role in determining the orientation of the clustering. For spherical non-deformable bubbles these authors simulated up to 216 bubbles with Reynolds numbers in the range of 12–30 and void fraction α up to 24 %, and Weber number of about 1. For the deformable case, they simulated 27 bubbles with Reynolds number of 26, Weber number of 3.7 and $\alpha = 6\,\%$. The authors found that the orientation of bubble clusters is strongly influenced by the deformability of the bubbles: spherical pairs of bubbles have a high probability of aligning horizontally, forming rafts, whereas the non-spherical ones preferentially align in the vertical orientation. In a later investigation, where inertial effects were more pronounced, Esmaeeli & Tryggvason (2005) studied both cases for bubble Reynolds number of order 100. In this case only a weak vertical cluster was observed in a swarm of 14 deformable bubbles. Their explanation for the weaker vertical clustering was that the wobbly bubble motion, enhanced by the larger Reynolds number, produces perturbations which do not allow the bubbles to align vertically and accelerate the breakup in case some of them cluster.

In spite of numerous experimental studies on pseudo-turbulence, bubble clustering has not yet been fully quantitatively analysed experimentally. Zenit *et al.* (2001) found a mild horizontal clustering using two-dimensional imaging techniques for bubbles with particulate Reynolds number higher than 100. Cartellier & Rivière (2001) studied the microstructure of homogeneous bubbly flows for Reynolds number of order 10. They found a moderate horizontal accumulation using pair density measurements with two optical probes. Their results showed a higher probability of the pair density in the horizontal plane and a reduced bubble density behind the wake of a test bubble. Risso & Ellingsen (2002) performed experiments with a swarm of deformable bubbles ($d_b = 2.5\,\mathrm{mm}$), aspect ratio around 2 and Reynolds number of 800. They did not find clustering and suggested that in this low void fraction regime ($\alpha < 1.05\,\%$) there was a weak influence of hydrodynamic interaction between bubbles.

1.2. *Mean bubble rise velocity and statistics of bubble velocity*

The mean bubble rise velocity in bubbly flows is found to decrease with increasing bubble concentration whereas the normalized vertical fluctuation $V_{z,rms}/\overline{V}_z$ increases (Zenit *et al.* 2001; Bunner & Tryggvason 2003; Martinez-Mercado, Palacios-Morales & Zenit 2007). The interpretation is that when increasing the concentration the

https://doi.org/10.1017/S0022112009993570 Published online by Cambridge University Press

bubble-induced counterflow becomes more important and in addition the hydrodynamic interactions between bubbles become more frequent and hinder the upward movement of bubbles, provoking at the same time, an increment of the bubble velocity fluctuations.

Next, probability density functions (PDFs) of bubble velocities provide useful information for effective force correlations used in bubbly flow models in industry. PDFs in pseudo-turbulence have been obtained in the numerical studies of Bunner & Tryggvason (2002*b*, 2003) and Esmaeeli & Tryggvason (2005). For non-deformable bubbles (Bunner & Tryggvason 2002*b*), the PDFs of velocity fluctuations have a Gaussian distribution. If deformability is considered (Bunner & Tryggvason 2003), the PDF of only one horizontal component of the velocity keeps a Gaussian shape while the non-Gaussianity in the PDFs was stronger at the lowest concentration $\alpha = 2\,\%$, recovering a Gaussian distribution for $\alpha = 6\,\%$. However in that numerical work only a limited number of bubbles ($N_b = 27$) could be considered and the different behaviour in the two different horizontal directions reflects the lack of statistical convergence. Experimental PDFs of bubble velocities in pseudo-turbulence have been obtained by Zenit *et al.* (2001) and by Martinez-Mercado *et al.* (2007). In these studies the bubble velocity was measured intrusively using an impedance probe technique. The amount of data points used for the PDFs was not sufficient for good statistical convergence.

1.3. *Liquid energy spectrum*

In bubbly flows, one must distinguish between the energy input due to the bubbles and the energy input due to some external forcing – either of them can be predominant. Lance & Bataille (1991) suggested the ratio of the bubble-induced kinetic energy and the kinetic energy of the flow without bubbles as an appropriate dimensionless number to characterize the type of the bubbly flow. Rensen, Luther & Lohse (2005) called this ratio the *bubblance* parameter b, defined as

$$b = \frac{1}{2}\frac{\alpha U_r^2}{u_0'^2}, \tag{1.1}$$

where α is already defined, U_r is the bubble rise velocity in still water and u_0' is the typical turbulent vertical fluctuation in the absence of bubbles. Lance & Bataille (1991) measured the liquid power spectrum in bubbly turbulence and observed a gradual change of the slope with increasing void fraction. At low concentrations the slope of the spectrum was close to the Kolmogorov turbulent value of $-5/3$. By increasing α, the principal driving mechanism changed – the forcing now more and more originated from the bubbles and not from some external driving. In that regime the slope was close to $-8/3$. Having in mind (1.1) one may expect different scaling behaviour, depending on the nature of the energy input that is dominant, namely $b < 1$ for dominant turbulent fluctuations or $b > 1$ for dominant bubble-induced fluctuations. Indeed from table 1 of Rensen *et al.* (2005) one may draw the conclusion that the slope is around $-5/3$ for $b < 1$ and around $-8/3$ for $b > 1$. Also Riboux, Risso & Legendre (2010) obtained a spectral slope of about -3 in the wake of a swarm of rising bubbles in still water ($b = \infty$). Moreover, in numerical simulations Sugiyama *et al.* (2001) obtained the same spectral slope for the velocity fluctuations caused by up to 800 rising light particles, i.e. $b = \infty$, with finite diameter ($Re \approx 30$). However, there are also counter-examples, e.g. Mudde, Groen & van der Akker (1997) and Cui & Fan (2004) obtained around $-5/3$, though $b = \infty$. Therefore, in this paper we want to re-examine the issue of the spectral slope in pseudo-turbulence ($b = \infty$).

https://doi.org/10.1017/S0022112009993570 Published online by Cambridge University Press

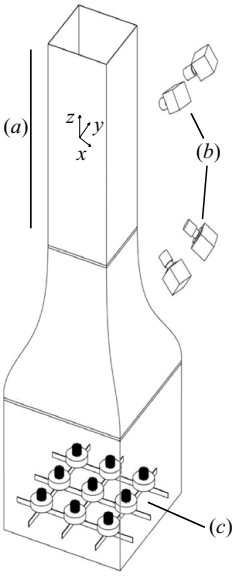


FIGURE 1. Experimental apparatus: (*a*) measurement section of length 2 m, (*b*) 4-camera PTV system, (*c*) capillary islands.

1.4. *Outline of the paper*

The paper is structured as follows: in § 2 the experimental apparatus is explained, and the particle tracking velocimetry (PTV) technique and phase-sensitive constant temperature anemometry (CTA) are described. Section 3 is divided in three subsections: in the first part results on bubble clustering are shown, followed by the results on the mean bubble rise velocity and the bubble velocity distributions and finally the power spectrum measurements are presented. Finally, a summary and an outlook on future work are presented in § 4.

2. Setup, tools and methods

2.1. *Twente water channel*

The experimental apparatus consists of a vertical water chunnel with a 2 m long measurement section with $0.45 \times 0.45\,\mathrm{m}^2$ cross-section. A sketch depicting the set-up is shown in figure 1. The measurement section has three glass walls for optical access and illumination (see Rensen *et al.* 2005 for more details). The channel was filled with deionized water to the top of the measurement section. The level of the liquid column was 3.8 m above the place where bubbles were injected. We used three capillary islands in the lowest part of the channel to generate bubbles. Each island contains 69 capillaries with an inner diameter of 500 μm. Different bubble concentrations were achieved by varying the air flow through the capillary islands. We performed experiments with dilute bubbly flows with typical void fractions in the range $0.28\,\% \leqslant \alpha \leqslant 0.74\,\%$ for PTV and in the range $0.20\,\% \leqslant \alpha \leqslant 2.2\,\%$ for CTA. The void fraction α was determined using a U-tube manometer which measures the pressure difference between two points at different heights of the measurement section (see Rensen *et al.* 2005). A mono-dispersed bubbly swarm with mean bubble diameter of 4–5 mm was studied. Typical Reynolds numbers Re are of the order 10^3, the Weber number We is in the range 2–3 (implying deformable bubbles) and

https://doi.org/10.1017/S0022112009993570 Published online by Cambridge University Press

α (%)	d_b (mm)	$\overline{V}_z$ (m s^{-1})	Re	We	Eo
0.28–0.74	4–5	0.16–0.22	1000	2–3	3–4

TABLE 1. Typical experimental parameters: void fraction α, mean bubble diameter ($d_b = \sqrt[3]{d_l^2 d_s}$), where d_l and d_s are the long and short axes of a two-dimensional image of a given ellipsoidal bubble, mean rising velocity in still water $\overline{V}_z$ and Reynolds ($Re = d_b\overline{V}_z/\nu_f$), Weber ($We = \rho d_b \overline{V}_z^2/\sigma$) and Eötvos ($Eo = \rho_f g d_b^2/\sigma$) numbers. Here $\nu_f = 1 \times 10^{-6}$ m^2 s^{-1} is the kinematic viscosity of water, $\sigma = 0.072$ N m^{-1} the surface tension at the air–water interface and g the gravitational acceleration.

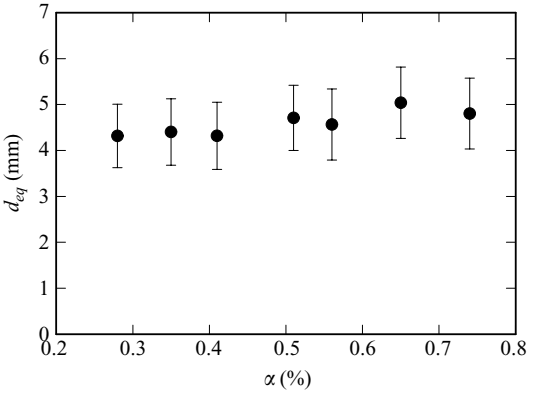


FIGURE 2. Equivalent bubble diameter d_{eq} as a function of void fraction α. Standard deviation as error bars. We measured the long d_l and short axes d_s of 400 bubbles per concentration from two-dimensional images. The equivalent diameter was obtained by assuming ellipsoidal bubbles with a volume equal to that of a spherical bubble, $d_{eq} = (d_s d_l^2)^{1/3}$.

the Eötvos number Eo is around 3–4. Table 1 defines these various dimensionless numbers and summarizes the experimental conditions. In figure 2, the mean bubble diameter d_{eq} as a function of void fraction is shown. The values are within the range of 4–5 mm and show a slight increment with bubble concentration.

2.2. *Particle tracking velocimetry*

In the last few years three-dimensional PTV has become a powerful measurement technique in fluid mechanics. The rapid development of high-speed imaging has enabled a successful implementation of the technique in studies on turbulent motion of particles (e.g. Mordant, Leveque & Pinton 2004; Guala *et al.* 2005; Berg *et al.* 2006; Bourgoin *et al.* 2006; Volk *et al.* 2008; Toschi & Bodenschatz 2009). The measured three-dimensional spatial position of particles and time trajectories allow a Lagrangian description which is the natural approach for transport mechanisms.

Figure 1 also sketches the positions of the four high-speed cameras (Photron 1024-PCI) which were used to image the bubbly flow. The four cameras were viewing from one side of the water channel and were focused in its central region, at a height of 2.8 m above the capillary islands. Lenses with 50 mm focal length were attached to the cameras. We had a depth of field of 6 cm. The image sampling frequency was 1000 Hz using a camera resolution of 1024×1024 pixel^2. The cameras were triggered externally in order to achieve a fully synchronized acquisition. We used the PTV

https://doi.org/10.1017/S0022112009993570 Published online by Cambridge University Press

α (%)	N_b	N_{link}	$N_{link}/N_b \cdot 100\,\%$
0.28	≈190	≈50	27
0.35	≈190	≈50	27
0.41	≈170	≈40	24
0.51	≈140	≈30	21
0.56	≈140	≈30	21
0.65	≈110	≈20	18
0.74	≈110	≈15	14

TABLE 2. Number of detected bubbles and linked bubbles per image for all concentrations studied. For the highest void fractions there is a drop in the number of linked bubbles, since most bubbles are imaged as two-dimensional merged blobs, which are not considered in the analysis.

software developed at ETH Zurich (Hoyer *et al.* 2005) for camera calibration and tracking algorithms. For a detailed description of this technique we refer to the work of Hoyer *et al.* (2005) and references therein. A three-dimensional solid target was used for calibration. Bubbles were detected within a volume of $16 \times 16 \times 6$ cm^3 with an accuracy of 400 µm. To illuminate the measuring volume homogeneous back-light and a diffusive plate were used in order to get the bubble's contour imaged as a dark shadow. The image sequence was binarized after subtracting a sequence-averaged background; then these images were used along with the PTV software to get the three-dimensional positions of the bubbles. We acquired 6400 images per camera corresponding to 6.4 s of measurement (6.7 Gbyte image files).

For higher bubble concentration, many bubbles are imaged as merged blobs and can not be identified as individual objects. These merged bubbles images are not considered for the analysis. Therefore the number N_b of clearly identified individual bubbles goes down with increasing void fraction. For the most dilute case ($\alpha = 0.28\,\%$) around $N_b \approx 190$ bubbles were detected in each image. This quantity dropped to nearly 100 for the most concentrated cases ($\alpha = 0.65\,\%$ and $\alpha = 0.74\,\%$). If a bubble is tracked in at least three consecutive time-steps, we call it a linked bubble. Table 2 summarizes typical values of number of bubbles (N_b) and linked bubbles (N_{link}) per image.

2.3. *Pair correlation function*

Particle clustering can be quantified using different mathematical tools like pair correlation functions (Bunner & Tryggvason 2002*a*), Lyapunov exponents (Bec *et al.* 2006*b*), Minkowski functionals (Calzavarini *et al.* 2008*b*) or PDFs of the distance between two consecutive bubbles in a time series (Calzavarini *et al.* 2008*a*). In this investigation the pair correlation function $G(r, \theta)$ is employed to understand how the bubbles are globally distributed. It is defined as follows:

$$G(r,\theta) = \frac{V}{N_b(N_b-1)} \left\langle \sum_{i=1}^{N_b} \sum_{j=1, i\neq j}^{N_b} \delta(\boldsymbol{r} - \boldsymbol{r}_{ij}) \right\rangle, \tag{2.1}$$

where V is the size of the calibrated volume, N_b is the number of bubbles within that volume, $\boldsymbol{r}_{ij}$ is the vector linking the centres of bubble i and bubble j and $\boldsymbol{r}$ is a vector with magnitude r and orientation θ, defined as the angle between the vertical unit vector and the vector linking the centres of bubbles i and j, as shown in figure 3. From (2.1), the radial and angular pair probability functions can be derived. To

https://doi.org/10.1017/S0022112009993570 Published online by Cambridge University Press

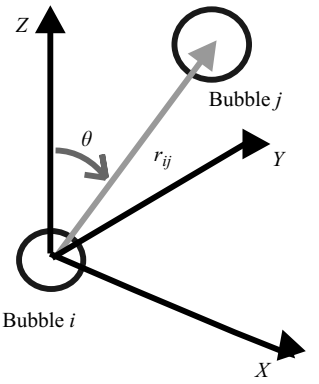


FIGURE 3. Definition of angle θ between a pair of neighbouring bubbles.

obtain the radial pair probability distribution function $G(r)$ one must integrate over spherical shells of radius r and width Δr, whereas for the angular pair probability distribution function $G(\theta)$ an r-integration is performed.

2.4. *Phase-sensitive constant-temperature anemometry*

Hot-film measurements in bubbly flows impose considerable difficulty due to the fact that liquid and gas information is present in the signal. The challenge is to distinguish and classify the signal corresponding to each phase. The hot-film probe does not provide by itself means for a successful identification. Thus many parametric and non-parametric signal processing algorithms have been used to separate the information on both phases, i.e. thresholding (Bruun 1995) or pattern recognition methods (Luther *et al.* 2005). The output of these algorithms is a constructed indicator function which labels the liquid and gas parts of the signal. We follow an alternative way and *measure* the indicator function, therefore avoiding uncertainties when computing it. This can be achieved by combining optical fibres for phase detection with the hot-film sensor (see Cartellier & Barrau 2001; Juliá *et al.* 2005).

The device, called phase-sensitive CTA, was firstly developed by van den Berg (2006). In this technique, an optical fibre is attached close to the hot-film probe so that when a bubble impinges onto the sensor it also interacts with the optical fibre. Its working principle is based on the different index of refraction of gas and liquid. A light source is coupled into the fibre. A photodiode measures the intensity of the light that is reflected from the fibre tip via a fibre coupler. The incident light leaves the tip of the fibre when immersed in water, but it is reflected back into the fibre when exposed to air, implying a sudden rise in the optical signal. Thus the intensity of the reflected light indicates the presence of either gas or liquid at the fibre's tip. In this way, if both signals are acquired simultaneously, the bubble collisions can straightforwardly be detected without the need of any signal-processing method. For the construction of the probe we used a DANTEC cylindrical probe (55R11) and attached two optical fibres to it (Thorlabs NA = 0.22 and 200 μm diameter core). We used two fibres in order to assure the detection of all bubbles interacting with the probe. The fibres were glued and positioned at the side of the cylindrical hot film, at a distance of about 1 mm from the hot film. An illustration of the hot film and fibres is shown in figure 4. The probe was put in the centre of the measurement section positioning its supporting arm parallel to the vertical rising direction of the bubbles so that the axis of the optical probes is also aligned with the preferential direction of

https://doi.org/10.1017/S0022112009993570 Published online by Cambridge University Press

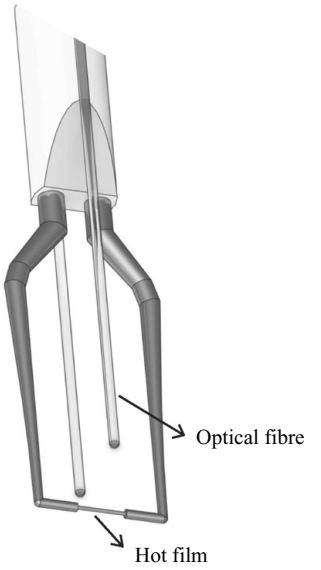


FIGURE 4. Phase-sensitive CTA probe with two attached optical fibres for bubble-probe detection.

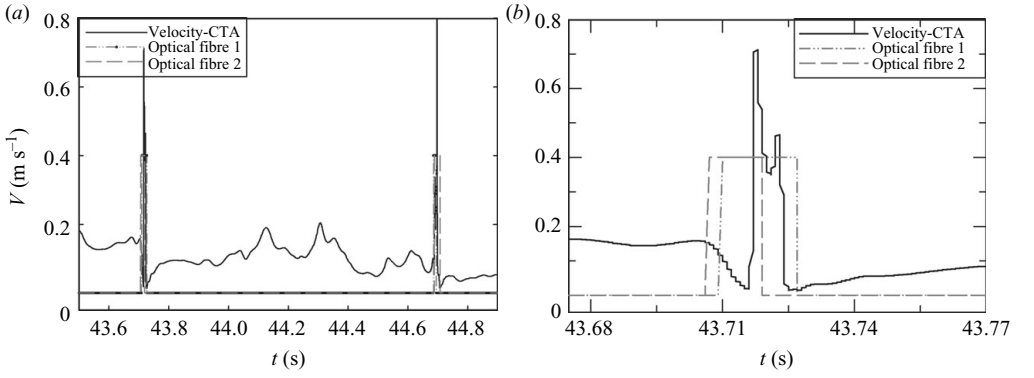


FIGURE 5. Typical phase-sensitive CTA signal already transformed into velocity. (*a*) Two consecutive bubble-probe interactions for $\alpha = 0.2\,\%$, (*b*) zoom in of a bubble collision.

the flow, thus allowing for a better bubble-probe interaction and aiming to minimize the slow down of bubbles approaching the probe. Van den Berg (2006) measured flow velocities with and without the fibre being attached to the probe. They found that the presence of the fibres does not compromise the probe's bandwidth and that its influence on the power spectrum is negligible.

With the signal of each optical fibre a discretized phase indicator function $\xi = \{\xi_i\}_{i=1}^{N}$ can be constructed, whose definition follows Bruun (1995), namely

$$\xi_i = \begin{cases} 1 & \text{liquid}, \\ 0 & \text{bubble}. \end{cases} \tag{2.2}$$

An unified phase indicator function is then obtained by multiplying the indicator functions of both fibres. A typical signal of phase-sensitive CTA with two consecutive bubble–probe interactions is shown in figure 5(*a*). There is one adjustable parameter

https://doi.org/10.1017/S0022112009993570 Published online by Cambridge University Press

to construct the indicator functions of the fibres. As explained above the phase discrimination can be done by an intensity threshold of the optical fibre's signal. When the rising edge of the signal exceeds this threshold, the indicator function of the fibre must change from a value 1 to 0, as defined in (2.2). If the optical fibre was positioned at the same place as the hot-film probe, the rising edge of its signal would occur precisely at the time when the bubble interacts with the hot film. However, there is a separation of about 1 mm between the fibres and the hot film, so that the rising edge of the optical fibres' signal occurs actually with some delay. Therefore, to construct the phase indicator function of the optical fibres, one must account for this delay and define the beginning of the interaction not where the signal exceeds the intensity threshold but some time before. The time used for this shifting was obtained by considering the vertical separation between the optical fibres and the hot-film probe and mean bubble velocities: in our experiment a bubble travels 1 mm in about 5–7 ms. We shifted the beginning of the collision 8 ms prior to the optical fibres' signal starts to rise from its base value. The shifting value was double checked by analysing the histograms of the duration of bubble collisions. As can be observed from figure 5(*b*), with this shift sometimes part of the CTA signal when the bubbles are approaching the probe ($<$10 ms) was lost, but we noticed no effect on the spectrum when varying the shift duration, provided the bubble spikes were still removed.

With the phase indicator function only pieces containing liquid information on the time series are used for further analysis – i.e. the part of the signal between the two bubble interactions shown in figure 5(*a*). For each part of the time series containing liquid information the spectrum was calculated. Then all spectra were averaged and the power spectrum for each bubble concentration was obtained. In this way neither an interpolation nor auto-regressive models for gapped time series were necessary. In our experiments the gas volume fractions varied from $0.2 \leqslant \alpha \leqslant 2.2\,\%$. The CTA was calibrated using a DANTEC LDA system (57N20 BSA). The calibration curve was obtained by fitting the data points to a fourth-order polynomial. The total measuring time was 1 h for each concentration and the sampling rate of the hot film and optical fibres was 10 kHz.

3. Bubble clustering and distributions in pseudo-turbulence

3.1. *Radial pair correlation*

The radial pair correlation $G(r)$ was obtained for all bubble concentrations studied. Figure 6 shows $G(r)$ as a function of the normalized radius $r^* = r/a$, where a is a mean bubble radius. As shown in figure 2 the mean equivalent bubble diameter is within the range 4–5 mm. Therefore we can normalize with one mean bubble radius and we picked $a = 2$ mm for all concentrations. We observe in figure 6 that the highest probability to find a pair of bubbles lies in the range of few bubble radii $r^* \approx 4$ for all concentrations. The probability $G(r)$ of finding a pair of bubbles within this range increases slightly with increasing α. For values $r^* < 2$ one would expect that $G(r) = 0$. However, in our experiments we found $G(r) \neq 0$ for $r^* < 2$, due to the fact that the bubbles are ellipsoidal and deform and wobble when rising.

We now estimate the error bar in the correlation function $G(r)$, originating from incomplete bubble detection, as seen from table 2. With increasing α the fraction of detected bubbles decreases. For $\alpha = 0.28\,\%$ we detect $N_b \approx 200$ so one would expect for $\alpha = 0.74\,\%$ to detect $N_b \approx (0.74/0.28) \times 200 \approx 500$ but we are detecting only 110, $\approx$20 % of them. In order to investigate the reliability of the pair correlation

https://doi.org/10.1017/S0022112009993570 Published online by Cambridge University Press

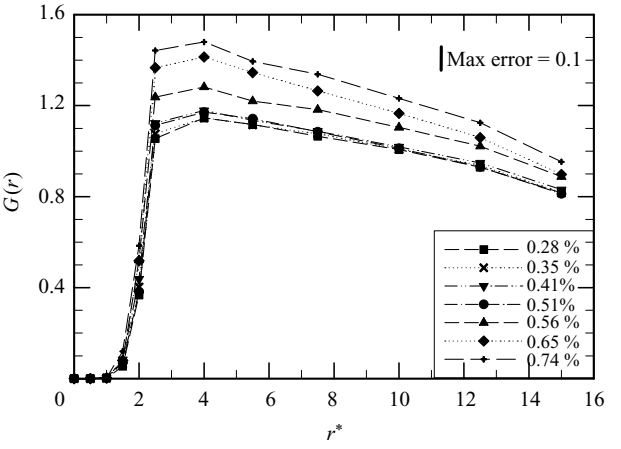


FIGURE 6. Radial pair probability $G(r)$ as a function of dimensionless radius r^*. The different curves are for different bubble volume concentrations α (given in per cent).

function due to this loss of bubble detection, we studied a set of randomly distributed particles. We generated 500 particles at 6000 times and calculated the radial and pair correlation functions, obtaining $G(r) = 1$ and $G(\theta) = 1$ as expected for randomly distributed particles. Then we kept only 20 % of the particles and recalculated the correlation functions to see how much they deviate from 1. We found that the maximum deviation was less than 0.1 for both the radial and the angular correlation functions. This is much smaller than the structure revealed in the $G(r)$ curve in figure 6. We therefore consider the clustering with the preferred distance of $r^* = 4$ as a robust feature of our data, in spite of incomplete bubble detection. In figure 6 this error bar corresponding to a maximum error of $G(r)$ at the most concentrated flow is also shown.

3.2. *Angular pair correlation*

The orientation of the bubble clustering was studied by means of the angular pair correlation $G(\theta)$ using different radii for the spherical sector over which neighbouring bubbles are counted. Figure 7(*a–c*) shows the results for $r^* = 40$, 15 and 5, respectively. The plots were normalized so that the area under the curve is unity. For all radii and concentrations, pairs of bubbles cluster in the vertical direction, as one can see from the highest peaks at $\theta/\pi = 0$ and $\theta/\pi = 1$. The value of $\theta/\pi = 0$ means that the reference bubble (at which the spherical sector is centred) rises below the pairing one. For $\theta/\pi = 1$ the reference bubble rises above the pairing bubble (see figure 3). When decreasing the radius of the spherical sector, i.e. when probing the short range interactions between the bubbles, we observe that a peak of the angular probability near $\pi/2$ starts to develop. The enhanced probability at this angle range is even more pronounced in figure 7(*c*) where the peak of $G(\theta)$ for horizontally aligned bubbles is just slightly lower than that for vertical clustering. It is worthwhile to point out that the vertical alignment of the bubbles is very robust and is present from very large to small scales, as the angular correlation for different spherical sectors is always higher at values $\theta/\pi = 0$ and 1 than at value $\theta/\pi = 0.5$. The maximum error bar for the angular correlation for the most concentrated flow at $\alpha = 0.74$ %, when 20 % of particles are detected, was 0.1 as explained above and is also shown in figure 7. It is much smaller than the structure of the signal.

https://doi.org/10.1017/S0022112009993570 Published online by Cambridge University Press

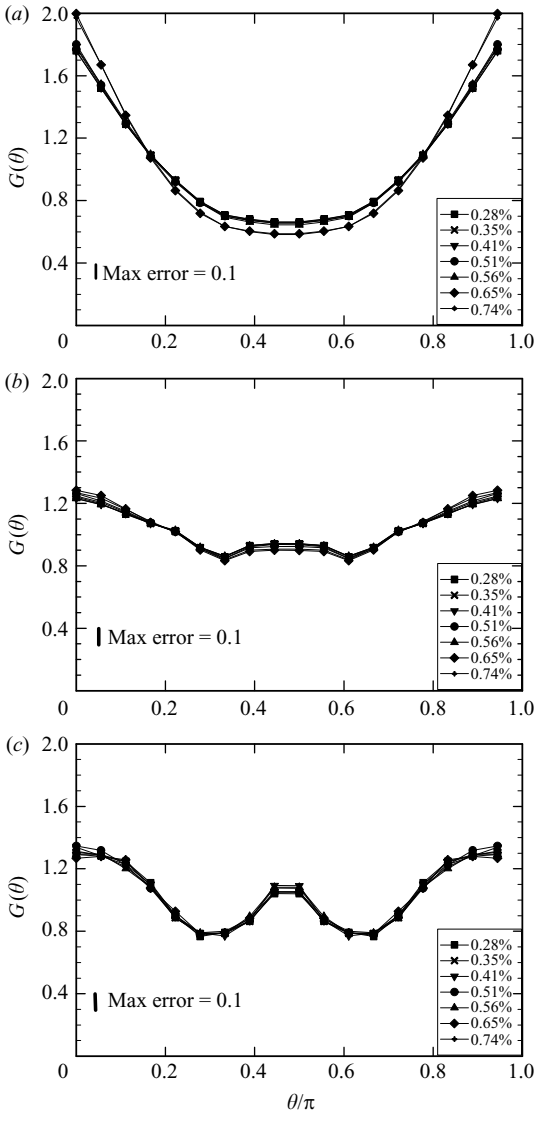


FIGURE 7. Normalized angular pair probability $G(\theta)$ as a function of angular position θ/π for various bubble concentrations α (see insets) and three different bubble-pair distances: (*a*) $r^* = 40$, (*b*) $r^* = 15$ and (*c*) $r^* = 5$. Maximum error bar for the angular correlation of 0.1 at $\alpha = 0.74\,\%$.

For comparison, we consider again the work of Bunner & Tryggvason (2003), who found that pairs of bubbles have a higher probability to align vertically, though for a much higher concentration ($\alpha = 6\,\%$) than employed here. Bunner & Tryggvason (2003) found that the vertical alignment was not as robust as in our case, since with increasing r^* the angular correlation at 0 and π became less dominant. Another significant difference between the findings of our experimental work and their simulations is that horizontal alignment was more pronounced with larger radii of the spherical sector and not when decreasing r^*. Our experimental results clearly show the main drawback and today's limitation when solving the flow at the particle's

https://doi.org/10.1017/S0022112009993570 Published online by Cambridge University Press

interface: the simulations are still restricted to a small number of particles, which is not sufficient to reveal long-range correlations.

3.3. *Interpretation of the clustering*

What is the physical explanation for a preferred vertical alignment of pairs of bubbles in pseudo-turbulence? Through potential flow theory, the mutual attraction of rising bubbles can be predicted (Batchelor 1967), but the application of potential theory to our experiments remains questionable (van Wijngaarden 1993), as we are in a statistically stationary situation where bubbles have already created vorticity. Our findings are consistent with the idea that deformability effects and the inversion of the lift force acting on the bubbles are closely related to the clustering. Mazzitelli, Lohse & Toschi (2003) showed numerically that it was mainly the lift force acting on point-like bubbles that makes them drift to the downflow side of a vortex in the bubble wake (see figure 2 in Mazzitelli *et al.* (2003) sketching the dynamics). Furthermore, when accounting for surface phenomena, Ervin & Tryggvason (1997) showed that the sign of the lift force inverts for the case of deformable bubbles in shear flow so that a trailing bubble is pulled into the wake of a leading bubble rather than expelled from it. In such a manner vertical rafts can be formed. Experimentally some evidence of the lift force inversion has been observed by Tomiyama *et al.* (2002) as lateral migration of bubbles under Poiseuille and Couette flow changed once the bubble size has become large enough. Numerical simulations of swarms of deformable bubbles without any flow predicted a vertical alignment (Bunner & Tryggvason 2003). An alternative interpretation of the results, due to Shu Takagi (Shu Takagi, private communication, 2009) goes as follows: small, pointwise, spherical bubbles have a small wake, allowing the application of potential flow. The bubbles then horizontally attract, leading to horizontal clustering. In contrast, large bubbles with their pronounced wake entrain neighbouring bubbles in their wake due to the smaller pressure present in those flow regions, leading to vertical clustering. Further efforts are needed to identify and confirm the main mechanism – i.e. either lift or pressure reduction in the bubble wake – leading to a preferential vertical alignment, for example, through experiments with small, spherical, non-deformable bubbles as achieved by Takagi, Ogasawara & Matsumoto (2008) through surfactants or with buoyant spherical particles.

3.4. *Average bubble rise velocity*

Bubble velocities were calculated by tracking the bubble positions which were linked in at least three consecutive images. The mean bubble rise velocity can thus be obtained as a function of the bubble concentration. Figure 8 shows the three components of the bubble velocity; the coordinate system corresponds to the one depicted in figure 1. The terminal rise velocity of a single bubble with $d_b = 3.9\,\mathrm{mm}$ and with the same water-impurity condition is also shown in figure 8, it has a value of $0.26\,\mathrm{m\,s^{-1}}$. A decrease in the mean bubble rise velocity with concentration is observed in our experiments within the experimental error shown in figure 8. The mean bubble rise velocity is $0.22\,\mathrm{m\,s^{-1}}$ for the most dilute case $\alpha = 0.28\,\%$ and decreases to a value of $0.16\,\mathrm{m\,s^{-1}}$ for $\alpha = 0.51\,\%$.

The interpretation of this finding is that in this parameter regime the velocity-reducing effect of the bubble-induced counterflow (see Batchelor 1972) and the scattering effect overwhelm the velocity-enhancing blob effect (originally suggested for sedimenting particles, Brenner 1999), implying that a blob of rising bubbles rises faster than a single one. For values of $\alpha \geqslant 0.56\,\%$ the mean values are again larger, around $0.18\,\mathrm{m\,s^{-1}}$. This increment of the mean rise velocity could be a result of our experimental error. As mentioned in § 2.2, the number of detected bubbles at higher

https://doi.org/10.1017/S0022112009993570 Published online by Cambridge University Press

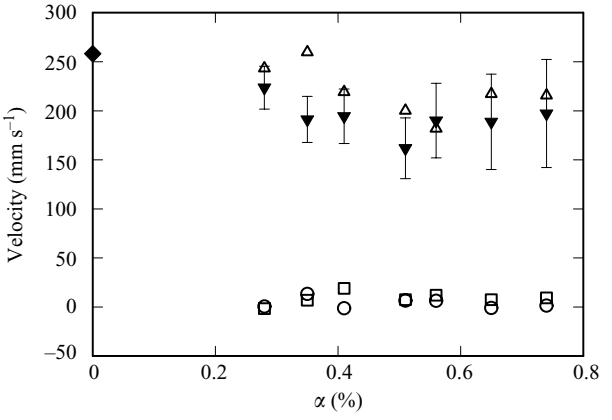


FIGURE 8. Mean bubble velocity as a function of bubble concentration α. All three components are shown: ○, V_x; □, V_y; ▼, mean bubble rise velocity $\overline{V}_z$; △, mean bubble rise velocity obtained by particle tracking from single camera two-dimensional images; ◆, terminal rise velocity for a single bubble with $d_b = 3.9$ mm. The error bars were obtained by estimating the 95 % confidence interval for the mean.

concentrations decreases by a factor 3 as compared to the most dilute cases. To check whether this increment was coming from detection of blobs of bubbles rather than single ones, we did experiments with a single camera positioned perpendicularly to the flow. The two-dimensional images were used to track bubbles manually making sure that the trajectories indeed corresponded to single bubbles. In figure 8 the mean bubble rise velocities from the one-camera two-dimensional analysis are plotted. A similar behaviour is observed, first a decrease with concentration, followed by a slight increase for the most concentrated flows, confirming the three-dimensional PTV results.

3.5. *Bubble velocity distributions*

Figure 9 shows the PDFs of all velocity components at the most dilute concentration ($\alpha = 0.28$ %). The number of data points used for calculating the PDFs was larger than 9×10^4 for the highest concentration $\alpha = 0.7$ % and of order 3×10^5 for the most dilute case. Even for the most concentrated flow, the number of data points was large enough to assure the statistical convergence of the PDFs. All PDFs show non-Gaussian features, as nicely revealed in the semi-log plot of the PDFs (figure 10).

In order to quantify the non-Gaussianity of the PDFs, the flatness values of the distributions were calculated. Their values are shown in the inset of figure 9 and are within the range 6–13. The flatness of the vertical component always has the highest values in the whole range of void fraction.

The effect of the concentration on the PDFs is also shown in figure 10. As in that figure the PDFs are shown on a semi-logarithmic scale so that the deviation from the Gaussian-like shape becomes more visible, it is revealed that there is no substantial change in the shape of the distributions with increasing bubble concentration.

We would like to compare the non-Gaussianity of the PDFs ('intermittency') found here with a comparable system, namely Rayleigh–Bénard convection as the analogy between buoyancy-driven bubbly flows and free thermal convection is interesting (see Climent & Magnaudet 1999). In Rayleigh–Bénard convection a fluid between two parallel plates is heated from below and cooled from above (see Ahlers, Grossmann & Lohse 2009 for a recent review). Prominent coherent structures in this system are thermal plumes, which are fluid particles either hotter or colder than the background

https://doi.org/10.1017/S0022112009993570 Published online by Cambridge University Press

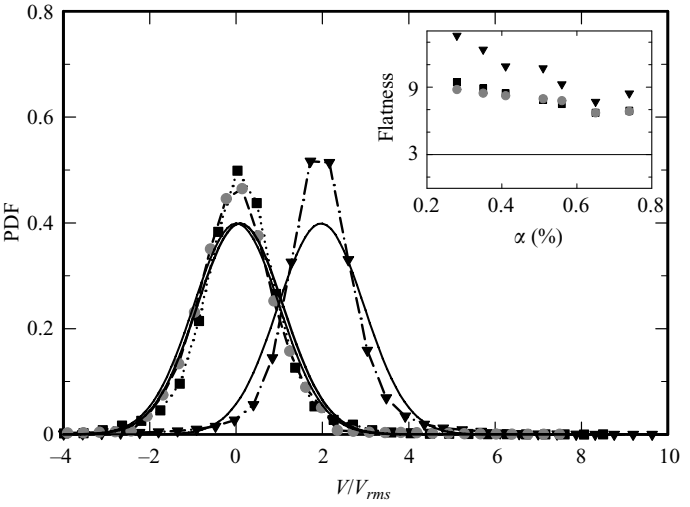


FIGURE 9. PDFs for the three bubble velocity components for $\alpha = 0.28\,\%$ normalized with the root mean square (r.m.s.) values of each component. V_x: dotted line with squares, V_y: dashed line with circles (both with V_{mean} velocities as expected), V_z: dotted-dashed line with triangles. The respective black solid lines (without symbols) show a Gaussian with the same mean and width as the measured distributions. The inset presents the flatness of the distribution as a function of the concentration α. The horizontal solid line in the inset represents the flatness for a normal distribution. Squares, triangles, and circles have the same meaning as in the main plot.

fluid. Due to the density difference with the background fluid, hotter plumes ascend and colder ones descend. The system is solely buoyancy-driven. Particularly, for large Pr (defined as the ratio of kinematic viscosity and thermal diffusivity of the working fluid) the plumes keep their integrity thanks to the small thermal diffusivity, so that the similarity with pseudo-turbulence is appealing. (We stress however that of course there are differences between the two systems which have been pointed out by Climent & Magnaudet 1999.)

Do the statistics of the velocity fluctuations in Rayleigh–Bénard convection share a similar behaviour with those of bubbles in pseudo-turbulence? In Rayleigh–Bénard convection, the PDF of the vertical velocity fluctuations of the background fluid – i.e. the central region of the cell – exhibits a Gaussian distribution (Daya & Ecke 2001). Qiu & Tong (2001) and Sun & Xia (2005) measured the vertical velocity fluctuations in the region where the plumes abound, and they found that the PDF still follows a Gaussian function. Those measurements, carried out for $Pr \approx 4$, indicate clearly that the PDF of the plume velocity fluctuations can be described by a Gaussian function, which differs significantly from the statistics of the bubble velocity in pseudo-turbulence. A possible reason for this difference could be that buoyancy in pseudo-turbulence is much stronger than that of the plumes in Rayleigh–Bénard system.

3.6. *Energy spectra of pseudo-turbulence*

Figure 11 shows the energy spectra for all gas fractions. As it can be seen, the slope of the energy spectrum hardly depends on the volume fraction – all curves show a slope of about -3.2. We stress that this scaling behaviour is maintained for nearly two decades, much wider than it had been reported in prior observations (Lance & Bataille 1991; Sugiyama *et al.* 2001; Riboux *et al.* 2010) of this steep slope of

https://doi.org/10.1017/S0022112009993570 Published online by Cambridge University Press

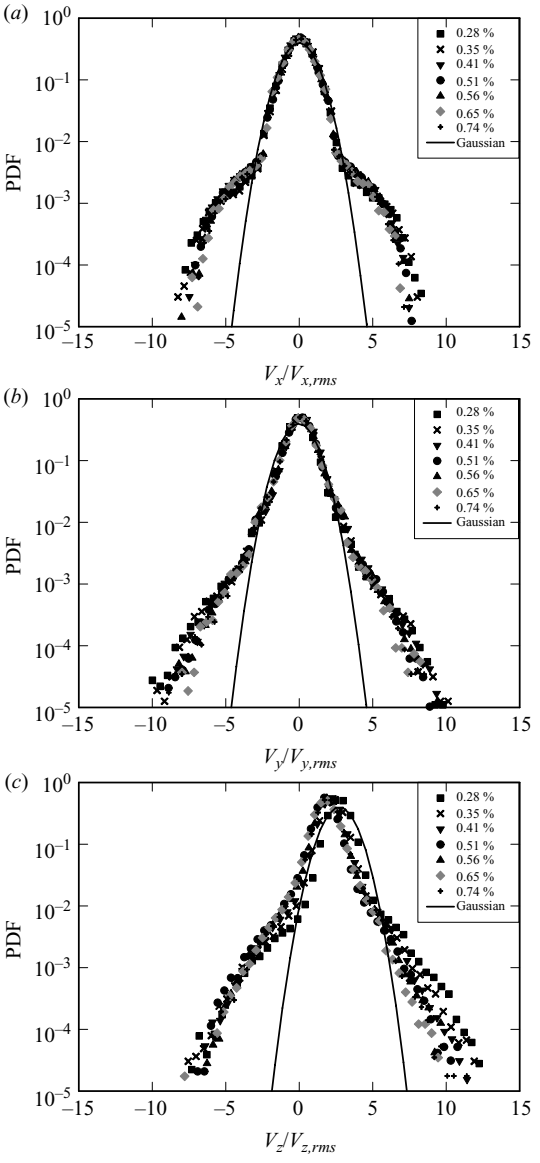


FIGURE 10. Same PDFs of the bubble velocity normalized with the r.m.s. values of each component as in figure 9, but now on a semi logarithmic scale to better reveal intermittency effects for various concentrations. As a reference, a Gaussian curve with the same mean and standard deviation as for the distribution with $\alpha = 0.28\,\%$ is plotted as a solid line.

pseudo-turbulence spectra. As was mentioned in § 2.4, the way the power spectrum was calculated in this investigation differs from previous ones in two aspects: firstly, the indicator function has been measured by means of the optical fibres; and secondly, an energy spectrum has been calculated for all individual liquid segments, before the final spectrum is obtained through averaging.

One wonders whether the duration of our interrupted time series is large enough to resolve the low frequency part of the spectrum: if the duration of these segments is too short, then indeed the low frequencies in the power spectrum can not be resolved.

https://doi.org/10.1017/S0022112009993570 Published online by Cambridge University Press

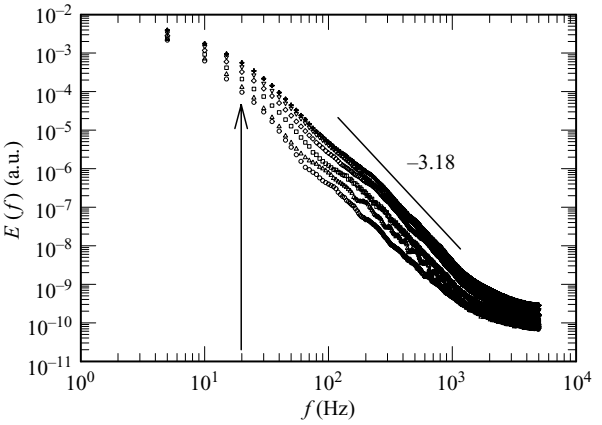


FIGURE 11. Liquid energy spectra for different void fractions. ○, $\alpha = 0.2\,\%$; △, $\alpha = 0.4\,\%$; □, $\alpha = 0.8\,\%$; ◇, $\alpha = 1.3\,\%$; ▽, $\alpha = 1.7\,\%$; +, $\alpha = 2.2\,\%$. The arrow shows the onset frequency of the scaling.

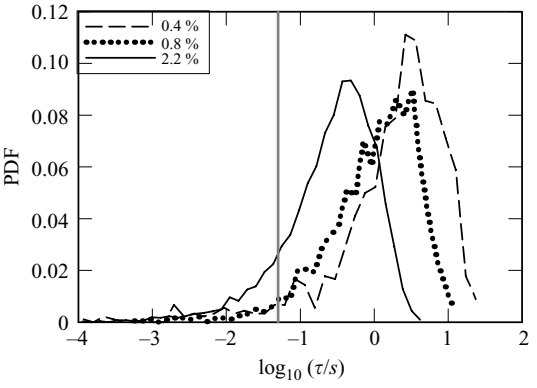


FIGURE 12. Distribution of the time duration of the parts containing liquid information in the CTA signal used to calculate the spectrum for three different bubble concentrations. The solid vertical line corresponds to the onset frequency of the scaling in figure 11, see arrow in that plot.

On the other hand, if the duration of the liquid segments is large enough, then all frequencies in the spectrum are well resolved. Figure 12 shows the distribution of the logarithm of the non-interrupted time series duration for three different concentrations. For $\alpha = 2.2\,\%$ (the most concentrated bubbly flow with more bubble–probe interaction, thus shorter liquid segments) around 90 % of the segments used to construct the spectrum have a duration larger than 0.05 s. Comparing with figure 11, we can see that for frequencies higher than 20 Hz we have resolved the inertial range, where the slope is ≈ -3.2. Thus the measurement of the spectra is consistent.

Why does the slope differ from the Kolmogorov value $-5/3$? One might expect a different scaling in pseudo-turbulence, as the velocity fluctuations are caused by the rising bubbles and not by the Kolmogorov–Richardson energy cascade, initiated by some large-scale motion. The difference between these two scalings is not yet completely understood, but there are some hypotheses on its origin. One possible explanation for the different scaling in pseudo-turbulence was given by Lance &

https://doi.org/10.1017/S0022112009993570 Published online by Cambridge University Press

Bataille (1991). They argued that eddies from the bubble wake are immediately dissipated before decaying towards smaller eddies, which would lead to the $-5/3$ scaling. They derived a -3 scaling, balancing the spectral energy, and assuming that the characteristic time of spectral energy transfer is larger than those of dissipation and production. More evidence that wake phenomena are related to the -3 scaling has been given by Risso *et al.* (2008) and by Roig & de Tournemine (2007). They showed that bubbles' wakes decay faster in pseudo-turbulence than in the standard turbulent case with the same energy and integral length scale. They also proposed a spatial and temporal decomposition of the fluctuations in order to gain more insight into the different mechanisms. In their experiments they used a fixed array of spheres. Very recently, Riboux *et al.* (2010) measured the spatial energy spectrum in pseudo-turbulence by means of PIV. They measured the spectrum just immediately after a bubble swarm has passed and obtained a -3 decay for wavelengths larger than the bubble diameter ($2\,\mathrm{mm} < l_c < 7\,\mathrm{mm}$). For wavelengths smaller than the bubble diameter they found that the spectrum recovered the $-5/3$ scaling. Their findings showed that the scaling is independent of the bubble diameter and void fraction in their range of parameters investigated ($0.2\,\% \leqslant \alpha \leqslant 12\,\%$ and $d_b = 1.6$–$2.5\,\mathrm{mm}$), which we also find. Their conclusion is that the -3 scaling is only a result of the hydrodynamic interactions between the flow disturbances induced by the bubbles. Their arguments for this statement are that the scaling appears for wavelengths larger than the bubble diameter and that a different scaling was found for smaller wavelengths. It is worthwhile to emphasize that in our case, we measured *within* the swarm where production is still maintained and steady. The -3 scaling in our measurements is in the range of 8 mm down to hundreds of micrometres (estimated by considering the mean bubble rise velocity and the starting and ending frequencies of the scaling of the spectrum in figure 11), thus for lengths not only larger than d_b but also for those up to one order of magnitude smaller than it. This supports that the dissipation of the bubble wake is involved and still a valid explanation for the -3 scaling as proposed by Lance & Bataille (1991). In any case, the papers by Sugiyama *et al.* (2001), Roig & de Tournemine (2007), Risso *et al.* (2008) and Riboux *et al.* (2010) and the present one show that the -3 scaling is typical for pseudo-turbulence.

One further result supporting this idea is the one obtained by Mazzitelli & Lohse (2009) who performed numerical simulations of microbubbles in pseudo-turbulence modelling them as point particles. Their DNS treated up to 288 000 bubbles, where near-field interactions were neglected, thus wake mechanisms can not be accounted for, and effective-force models were used for the drag and lift forces. They obtained a slope of the power spectrum close to $-5/3$ typical for the turbulent case. This gives evidence that the bubble's wake – missing in the point particle approach – and its dissipation play a very important role in the -3 scaling of the energy spectrum in pseudo-turbulence.

4. Summary

We performed experiments on bubble clustering using three-dimensional PTV. This is the first time that the technique has been used to investigate bubbly flows in pseudo-turbulence in very dilute regimes ($\alpha < 1\,\%$). Bubble positions were determined to study bubble clustering and alignment. For that purpose the pair correlation function $G(r, \theta)$ was calculated. As the radial correlation $G(r)$ shows, pairs of bubbles cluster within a few bubble radii $2.5 < r^* < 4$. Varying the bubble concentration does not have any effect on the clustering distance. The angular pair correlation $G(\theta)$

https://doi.org/10.1017/S0022112009993570 Published online by Cambridge University Press

shows that a robust vertical alignment is present at both small and large scales, as it is observed when varying the radius of the spherical sector ($r^* = 40$, 15 and 5). Decreasing the radius of the spherical sector shows that horizontal clustering also occurs, as the peak of the angular correlation around $\pi/2$ starts to grow with decreasing values of r^*.

PDFs of bubble velocity show that all components of bubble velocity behave differently from Gaussian. The implementation of this non-intrusive imaging technique assures enough data points to obtain convergence in PDFs. The improvement achieved in the number of data points, compared with previous experimental investigations, is of order 10^2. Furthermore, this allowed us to show the intermittent signature that bubble distributions have for all components. The flatness values for these velocity distributions are in the range of 6–13. The distribution of the rise velocity showed the highest values of flatness, e.g. ≈ 13 at $\alpha = 0.28\,\%$. The non-Gaussianity can be a result of the cluster formation mechanism, where the rise velocity of single bubbles is affected by the faster collective motion of clusters. However further investigations are needed to fully understand its origin.

We have shown that the power spectrum in pseudo-turbulence ($b = \infty$) decays exponentially with a slope near -3 which is consistent with the theoretical scaling that Lance & Bataille (1991) derived and supporting the hypothesis that bubble wake mechanisms are closely related to it. We have shown that the implementation of phase-sensitive CTA for studying bubbly flows is of great advantage, allowing a direct recognition and discarding of bubble–probe interactions.

The next step of our research will be to investigate bubble clustering for $b \ll 1$, where turbulent effects become dominant. Another line of research is to analyse pseudo-turbulence with smaller bubbles (e.g. achieved by surfactants Takagi *et al.* 2008), to study the effect of the length scale of the bubble on the spectra.

We thank specially Gert-Wim Bruggert, Martin Bos and Bas Benschop for their invaluable help with the experimental apparatus. We thank Lorenzo del Castello, Beat Lüthi and Haitao Xu for all the help and discussions regarding the PTV system, Frédéric Risso, Veronique Roig and Roberto Zenit for the discussion on energy spectra in pseudo-turbulence, Rob Mudde for help and discussion on probe related issues, Shu Takagi, Yoichiro Matsumoto and Bert Vreman. Special thanks for one of the referees for his/her constructive and helpful comments on the pair correlation function. This research is part of the Industrial Partnership Programme: *Fundamentals of heterogeneous bubbly flows* which is funded by the Stichting voor Fundamenteel Onderzoek der Materie (FOM).

REFERENCES

Ahlers, G., Grossmann, S. & Lohse, D. 2009 Heat transfer and large scale dynamics in turbulent Rayleigh–Bénard convection. *Rev. Mod. Phys.* **81**, 503–537.

Ayyalasomayajula, S., Gylfason, A., Collins, L. R., Bodenschatz, E. & Warhaft, Z. 2006 Lagrangian measurements of inertial particle accelerations in grid generated wind tunnel turbulence. *Phys. Rev. Lett.* **97**, 144507.

Batchelor, G. K. 1967 *An Introduction of Fluid Dynamics*. Cambridge University Press.

Batchelor, G. K. 1972 Sedimentation in a dilute dispersion of spheres. *J. Fluid Mech.* **52**, 245–268.

Bec, J., Biferale, L., Boffetta, G., Celani, A., Cencini, M., Lanotte, A., Musacchio, S. & Toschi, F. 2006*a* Accelerations statistics of heavy particles in turbulence. *J. Fluid Mech.* **550**, 349–358.

Bec, J., Biferale, L., Boffetta, G., Cencini, M., Musacchio, S. & Toschi, F. 2006*b* Lyapunov exponents of heavy particles in turbulence. *Phys. Fluids* **18**, 091702.

https://doi.org/10.1017/S0022112009993570 Published online by Cambridge University Press

Berg, J., Lüthi, B., Mann, J. & Ott, S. 2006 Backwards and forwards relative dispersion in turbulent flow: an experimental investigation. *Phys. Rev.* E **74**, 016304.

van den Berg, T. H. 2006 The effect of bubbles on developed turbulence. PhD Thesis, University of Twente, The Netherlands.

Bourgoin, M., Ouellette, N. T., Xu, H., Berg, T. & Bodenschatz, E. 2006 The role of pair dispersion in turbulent flow. *Science* **311**, 835–838.

Brenner, M. P. 1999 Screening mechanisms in sedimentation. *Phys. Fluids* **11**, 754–772.

Bruun, H. H. 1995 *Hot Wire Anemometry: Principles and Signal Analysis*. Oxford University Press.

Bunner, B. & Tryggvason, G. 2002*a* Dynamics of homogeneous bubbly flows. Part 1. Rise velocity and microstructure of the bubbles. *J. Fluid Mech.* **466**, 17–52.

Bunner, B. & Tryggvason, G. 2002*b* Dynamics of homogeneous bubbly flows. Part 2. Velocity fluctuations. *J. Fluid Mech.* **466**, 53–84.

Bunner, B. & Tryggvason, G. 2003 Effect of bubble deformation on the properties of bubbly flows. *J. Fluid Mech.* **495**, 77–118.

Calzavarini, E., van der Berg, T. H., Toschi, F. & Lohse, D. 2008*a* Quantifying microbubble clustering in turbulent flow from single-point measurements. *Phys. Fluids* **20**, 040702.

Calzavarini, E., Kerscher, M., Lohse, D. & Toschi, F. 2008*b* Dimensionality and morphology of particle and bubble clusters in turbulent flow. *J. Fluid Mech.* **607**, 13–24.

Cartellier, A. & Barrau, E. 2001 Monofiber optical probes for gas detection and gas velocity measurements: conical probes. *Intl J. Multiphase Flows* **24**, 1265–1294.

Cartellier, A. & Rivière, N. 2001 Bubble-induced agitation and microstructure in uniform bubbly flows at small to moderate particle Reynolds number. *Phys. Fluids* **13**, 8.

Climent, E. & Magnaudet, J. 1999 Large-scale simulations of bubble-induced convection in a liquid layer. *Phys. Rev. Lett.* **82** (24), 4827–4830.

Cui, Z. & Fan, L. S. 2004 Turbulence energy distributions in bubbling gas–liquid and gas–liquid–solid flow systems. *Chem. Engng Sci.* **59**, 1755–1766.

Daya, Z. A. & Ecke, R. E. 2001 Does turbulent convection feel the shape of the container? *Phys. Rev. Lett.* **87**, 184501.

Deckwer, B. D. 1992 *Bubble Column Reactors*, 1st edn. Wiley.

Ervin, E. A. & Tryggvason, G. 1997 The rise of bubbles in a vertical shear flow. *J. Fluids Engng* **119**, 443–449.

Esmaeeli, A. & Tryggvason, G. 2005 A direct numerical simulation study of the buoyant rise of bubbles at $O(100)$ Reynolds number. *Phys. Fluids* **17**, 093303.

Guala, M., Liberzon, A., Lüthi, B., Tsinober, A. & Kinzelbach, W. 2005 On the evolution of material lines and vorticity in homogeneous turbulence. *Phys. Rev.* E **533**, 339–359.

Hoyer, K., Holzner, M., Luethi, B., Guala, M., Liberzon, A. & Kinzelbach, W. 2005 three-dimensional scanning particle tracking velocimetry. *Exps. Fluids* **39**, 923–934.

Juliá, J. E., Harteveld, W. K., Mudde, R. F. & van der Akker, H. E. A. 2005 On the accuracy of the void fraction measurements using optical probes in bubbly flows. *Rev. Sci. Instrum.* **76**, 035103.

Kok, J. B. W. 1993 Dynamics of a pair of bubbles moving through liquid. Part 1. Theory. *Eur. J. Mech.* B **12**, 515–540.

Lance, M. & Bataille, J. 1991 Turbulence in the liquid phase of a uniform bubbly water–air flow. *J. Fluid Mech.* **222**, 95–118.

Luther, S., Rensen, J., van den Berg, T. H. & Lohse, D. 2005 Data analysis for hot-film anemometry in turbulent bubbly flow. *Exp. Therm. Fluid Sci.* **29**, 821.

Mazzitelli, I. M. & Lohse, D. 2009 Evolution of energy in flow driven by rising bubbles. *Phys. Rev.* E **79** (6), 066317.

Mazzitelli, I. M., Lohse, D. & Toschi, F. 2003 The effect of microbubbles on developed turbulence. *Phys. Fluids* **15**, L5–L8.

Martínez-Mercado, J., Palacios-Morales, C. & Zenit, R. 2007 Measurements of pseudoturbulence intensity in monodispersed bubbly liquids for $10 < \mathrm{Re} < 500$. *Phys. Fluids* **19**, 103302.

Mordant, N., Leveque, E. & Pinton, J. F. 2004 Experimental and numerical study of the Lagrangian dynamics of high Reynolds turbulence. *New J. Phys.* **6** (116), 1–44.

https://doi.org/10.1017/S0022112009993570 Published online by Cambridge University Press

Mudde, R. F., Groen, J. S. & van der Akker, H. E. A. 1997 Liquid velocity field in a bubble column: LDA experiments. *Chem. Engng Sci.* **52**, 4217–4224.

Qiu, X. L. & Tong, P. 2001 Large-scale velocity structures in turbulent thermal convection. *Phys. Rev.* E **64**, 036304.

Rensen, J., Luther, S. & Lohse, D. 2005 The effects of bubbles on developed turbulence. *J. Fluid Mech.* **538**, 153–187.

Riboux, G., Risso, F. & Legendre, D. 2010 Experimental characterization of the agitation generated by bubbles rising at high Reynolds number. *J. Fluid Mech.* (in press).

Risso, F. & Ellingsen, K. 2002 Velocity fluctuations in a homogeneous dilute dispersion of high-Reynolds-number rising bubbles. *J. Fluid Mech.* **453**, 395–410.

Risso, F., Roig, V., Amoura, Z., Riboux, G. & Billet, A. M. 2008 Wake attenuation in large Reynolds number dispersed two-phase flows. *Phil. Trans. R. Soc.* A **366**, 2177–2190.

Roig, V. & de Tournemine, L. 2007 Measurement of interstitial velocity of homogeneous bubbly flows at low to moderate void fraction. *J. Fluid Mech.* **572**, 87–110.

Salazar, J. P. L. C., de Jong, J., Cao, L., Woodward, S. H., Meng, H. & Collins, L. R. 2008 Experimental and numerical investigation of inertial particle clustering in isotropic turbulence. *J. Fluid Mech.* **600**, 245–256.

Sangani, A. S. & Didwana, A. K. 1993 Dynamic simulations of flows of bubbly liquids at large Reynolds numbers. *J. Fluid Mech.* **250**, 307–337.

Saw, E. W., Shaw, R. A., Ayyalasomayajula, S., Chuang, P. Y. & Gylfason, A. 2008 Inertial clustering of particles in high-Reynolds-number turbulence. *Phys. Rev. Lett.* **100**, 214501.

Smereka, A. S. 1993 On the motion of bubbles in a peridic box. *J. Fluid Mech.* **254**, 79–112.

Sugiyama, K., Takagi, S. & Matsumoto, Y. 2001 Multi-scale analysis of bubbly flows. *Comput. Methods Appl. Mech. Engng* **191** (6–7), 689 –704.

Sun, C. & Xia, K. Q. 2005 Scaling of the Reynolds number in turbulent thermal convection. *Phys. Rev.* E **72**, 067302.

Takagi, S., Ogasawara, T. & Matsumoto, Y. 2008 The effects of surfactant on the multiscale structure of bubbly flows. *Phil. Trans. R. Soc. Lond.* A **366** (1873), 2117–2129.

Tomiyama, A., Tamai, H., Zun, I. & Hosokawa, S. 2002 Transverse migration of single bubbles in simple shear flows. *Chem. Engng Sci.* **57** (11), 1849–1858.

Toschi, F. & Bodenschatz, E. 2009 Lagrangian properties of particles in turbulence. *Annu. Rev. Fluid Mech.* **41**, 375–404.

Volk, R., Calzavarini, E., Verhille, G., Lohse, D., Mordant, N., Pinton, J. F. & Toschi, F. 2008 Acceleration of heavy and light particles in turbulence: comparison between experiments and direct numerical simulations. *Physica* D **237** (14–17), 2084–2089.

van Wijngaarden, L. 1993 The mean rise velocity of pairwise-interacting bubbles in liquid. *J. Fluid Mech.* **251**, 55–78.

van Wijngaarden, L. 2005 Bubble velocities induced by trailing vortices behind neighbours. *J. Fluid Mech.* **541**, 203–229.

Zenit, R., Koch, D. L. & Sangani, A. S. 2001 Measurements of the average properties of a suspension of bubbles rising in a vertical channel. *J. Fluid Mech.* **429**, 307–342.

https://doi.org/10.1017/S0022112009993570 Published online by Cambridge University Press